GEOPHYSICS, VOL. 83, NO. 4 (JULY-AUGUST 2018); P. T235–T244, 11 FIGS., 2 TABLES.
10.1190/GEO2017-0535.1

A discontinuous-grid finite-difference scheme for frequency-domain 2D scalar wave modeling

Na Fan[1], Lian-Feng Zhao[2], Xiao-Bi Xie[3], and Zhen-Xing Yao[2]

ABSTRACT

The discontinuous-grid method can greatly reduce the storage requirement and computational cost in finite-difference modeling, especially for models with large velocity contrasts. However, this technique is mostly applied to time-domain methods. We have developed a discontinuous-grid finite-difference scheme for frequency-domain 2D scalar wave modeling. Special frequency-domain finite-difference stencils are designed in the fine-coarse grid transition zone. The coarse-to-fine-grid spacing ratio is restricted to 2^n, where n is a positive integer. Optimization equations are formulated to obtain expansion coefficients for irregular stencils in the transition zone. The proposed method works well when teamed with commonly used 9- and 25-point schemes. Compared with the conventional frequency-domain finite-difference method, the proposed discontinuous-grid method can largely reduce the size of the impedance matrix and number of nonzero elements. Numerical experiments demonstrated that the proposed discontinuous-grid scheme can significantly reduce memory and computational costs, while still yielding almost identical results compared with those from conventional uniform-grid simulations. When tested for a very long elapsed time, the frequency-domain discontinuous-grid method does not show instability problems as its time-domain counterpart usually does.

INTRODUCTION

Compared with time-domain finite-difference (TDFD) modeling, the frequency-domain finite-difference (FDFD) method presents numerous advantages, including fewer accumulative errors that can cause stability problems, flexibility in calculating a single frequency or a few frequencies, generating responses from multiple shots using a direct solver, or implementation of anelasticity by directly introducing complex constitutive relations (Jo et al., 1996; Chen, 2012; Gosselin-Cliche and Giroux, 2014; Li et al., 2016). An efficient solver for the wave equation is the basis for frequency-domain seismic reverse time migration or full-waveform inversion (Loewenthal and Mufti, 1983; Pratt, 1999; Plessix and Mulder, 2004; Brossier et al., 2009; Virieux and Operto, 2009; Kim et al., 2011). Many researchers have successfully developed FDFD operators and optimal methods, e.g., the rotated FD method, weighed-average method, and average-derivative method (e.g., Jo et al., 1996; Shin and Sohn, 1998; Štekl and Pratt, 1998; Min et al., 2000; Hustedt et al., 2004; Operto et al., 2007, 2009, 2014; Cao and Chen, 2012; Chen, 2012, 2014; Gu et al., 2013; Gosselin-Cliche and Giroux, 2014; Zhang et al., 2014, 2015; Tang et al., 2015; Chen and Cao, 2016; Yang and Mao, 2016; Fan et al., 2017). One of the major drawbacks in these techniques is the computational cost due to implicitly solving the linear equations, and this limits its practical applications. Therefore, it is always desirable to improve the efficiency in frequency-domain forward modeling.

For numerical modeling methods based on grid discretization, the spatial and temporal sampling intervals are major factors affecting the modeling accuracy and efficiency. Undersampling results in inaccurate solutions and unacceptable numerical dispersion, whereas oversampling can cause storage and computational overburdens (Tessmer, 2000; Hu and Jia, 2016). This dilemma occurs especially for media with large velocity variations. Therefore, it is desirable to adapt samplings to model velocity and signal frequency. For TDFD modeling, the nonuniform grid with variable spacing, discontinuous grid (e.g., Jastram and Behle, 1992; Wang and Schuster, 1996; Wang et al., 2001; Kristek et al., 2010; Zhang et al., 2013; Fan et al.,

Manuscript received by the Editor 12 August 2017; revised manuscript received 13 March 2018; published ahead of production 17 April 2018; published online 25 June 2018.
[1]Yangtze University, School of Geophysics and Oil Resources, Key Laboratory of Exploration Technologies for Oil and Gas Resources of Ministry of Education, Wuhan, China and Hubei Cooperative Innovation Center of Unconventional Oil and Gas, Wuhan, China. E-mail: fannachina@hotmail.com.
[2]Institute of Geology and Geophysics, Chinese Academy of Sciences, Key Laboratory of Earth and Planetary Physics, Beijing, China. E-mail: zhaolf@mail.iggcas.ac.cn; yaozx@mail.iggcas.ac.cn.
[3]University of California at Santa Cruz, Institute of Geophysics and Planetary Physics, Santa Cruz, California, USA. E-mail: xxie@ucsc.edu.

2015; Li et al., 2015), or variable time steps (e.g., Falk et al., 1998; Tessmer, 2000; Kang and Baag, 2004; Huang and Dong, 2009a, 2009b; Li et al., 2015) have been developed to increase the computation efficiency. FDFD modeling discretizes the wave equation in the frequency and spatial domains simultaneously. Therefore, there exist two types of nonuniform grids, the frequency-adaptive grid and the space-adaptive grid. The former adopts a coarse grid at high frequencies and a fine grid at low frequencies, and the spatial interval usually decreases as the frequency increase (Fichtner et al., 2013; Hu and Jia, 2016). The latter, also known as the velocity-adaptive grid, is widely used in TDFD modeling (e.g., Jastram and Behle, 1992; Jastram and Tessmer, 1994; Wang and Schuster, 1996; Aoi and Fujiwara, 1999; Hayashi et al., 2001; Wang and Takenaka, 2001; Wang et al., 2001; Kang and Baag, 2004; Kristek et al., 2010; Zhang et al., 2013; Fan et al., 2015; Li et al., 2015), but it is seldom used in FDFD modeling. The space-adaptive grid scheme is proposed to save computational cost for models with large velocity contrasts. It uses fine and coarse grids to discretize low- and high-velocity areas, respectively. The major issue for the space-adaptive nonuniform grid is dealing with the wavefield in the transition zone between two grids, where, without proper FD schemes, artificial reflections may be generated (Fan et al., 2015).

A recently developed technique is the mesh-free FD (e.g., Martin et al., 2015; Takekawa et al., 2015; Takekawa and Mikada, 2016; Li et al., 2017), which is highly adaptive to complex velocity variations and model geometry but also has certain disadvantages. To approximate the spatial derivatives, the mesh-free FD usually requires more neighboring nodes compared with conventional FD, and weighting coefficients vary from node to node. Much information (e.g., the locations of individual nodes and their neighbors and the weighting coefficients for all of the surrounding nodes) has to be saved (Li et al., 2017). Moreover, to generate the node layout is not easy work (Fornberg and Flyer, 2015). Therefore, the merits of this method have yet to be investigated.

As another option, we propose a frequency-domain discontinuous-grid FD, in which rectangular lattices are used in the major computation areas. Only in very limited areas, where the lattices need to transfer from one density to another, are special stencils required. This method can achieve a moderate capability to adapt to velocity variations, while keeping a lot of convenience similar to conventional FDFD. In the following sections, we will first present our methodology. Then, we give numerical examples to demonstrate the theoretical analysis, and finally make the conclusion.

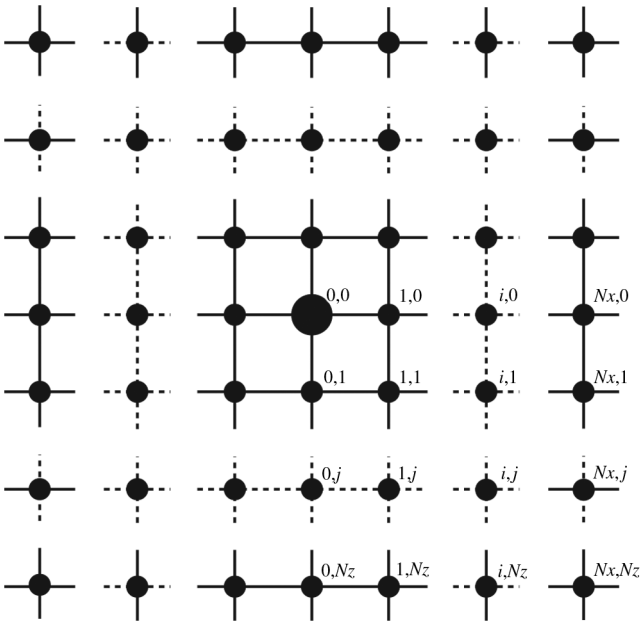

Figure 1. Schematic stencil of the 2D FDFD operator.

THEORY

The frequency-domain finite-difference operator

The 2D scalar wave equation in the frequency domain is given by

$$\frac{\partial^2 P}{\partial x^2}+\frac{\partial^2 P}{\partial z^2}+\frac{\omega^2}{v^2}P=0, \tag{1}$$

where P is the pressure, ω is the angular frequency, and v is the velocity. Given an FDFD operator with $(2N_x+1)\times(2N_z+1)$ points around the central point (Figure 1), the approximation of the spatial derivatives is (Fan et al., 2017)

$$\frac{\partial^2 P}{\partial x^2}\approx\frac{1}{\Delta x^2}\sum_{i=0}^{N_x}\sum_{j=0}^{N_z}c_{i,j}(P_{m-i,n-j}+P_{m+i,n+j}+P_{m-i,n+j}+P_{m+i,n-j}), \tag{2a}$$

$$\frac{\partial^2 P}{\partial z^2}\approx\frac{1}{\Delta z^2}\sum_{i=0}^{N_x}\sum_{j=0}^{N_z}d_{i,j}(P_{m-i,n-j}+P_{m+i,n+j}+P_{m-i,n+j}+P_{m+i,n-j}), \tag{2b}$$

where $P_{m,n}=P(m\Delta x,n\Delta z)$, Δx and Δz are the spatial sampling intervals in the x- and z-directions; $c_{i,j}$ and $d_{i,j}$ are the weighting coefficients satisfying $\sum_{i=0}^{N_x}\sum_{j=0}^{N_z}c_{i,j}=0$ and $\sum_{i=0}^{N_x}\sum_{j=0}^{N_z}d_{i,j}=0$; and subscripts i, j identify the locations shown in Figure 1. The mass acceleration term in equation 1 can be written as

$$\frac{\omega^2}{v^2}P=\frac{\omega^2}{v^2}\sum_{i=0}^{N_x}\sum_{j=0}^{N_z}b_{i,j}(P_{m-i,n-j}+P_{m+i,n+j}+P_{m-i,n+j}+P_{m+i,n-j}), \tag{3}$$

where $b_{i,j}$ satisfy $\sum_{i=0}^{N_x}\sum_{j=0}^{N_z}b_{i,j}=\frac{1}{4}$ with $(b_{i,j}\geq 0)$. Substituting equations 2 and 3 into equation 1, we obtain the general FDFD scheme for 2D scalar wave equation:

$$\begin{aligned}&\frac{1}{\Delta x^2}\sum_{i=0}^{N_x}\sum_{j=0}^{N_z}c_{i,j}(P_{m-i,n-j}+P_{m+i,n+j}+P_{m-i,n+j}+P_{m+i,n-j})\\&+\frac{1}{\Delta z^2}\sum_{i=0}^{N_x}\sum_{j=0}^{N_z}d_{i,j}(P_{m-i,n-j}+P_{m+i,n+j}+P_{m-i,n+j}+P_{m+i,n-j})\\&+\frac{\omega^2}{v^2}\sum_{i=0}^{N_x}\sum_{j=0}^{N_z}b_{i,j}(P_{m-i,n-j}+P_{m+i,n+j}+P_{m-i,n+j}+P_{m+i,n-j})=0.\end{aligned} \tag{4}$$

When $\Delta x\neq\Delta z$, the quantity G (the number of grid points per wavelength) is defined with respect to the larger spatial sampling interval $\max(\Delta x,\Delta z)$. Therefore, we separate the analysis for $\Delta x\geq\Delta z$

and $\Delta x < \Delta z$. We only need to consider the case $\Delta x \geq \Delta z$, and the case $\Delta x < \Delta z$ can be treated using the similar method (refer to Fan et al., 2017). By substituting the aspect ratio $r = \Delta x/\Delta z$ into equation 4 and letting $a_{i,j} = c_{i,j} + r^2 d_{i,j} (i = 0,1, \cdots N_x, j = 0,1, \cdots N_z)$, we obtain

$$\frac{1}{\Delta x^2}\sum_{i=0}^{N_x}\sum_{j=0}^{N_z} a_{i,j}(P_{m-i,n-j}+P_{m+i,n+j}+P_{m-i,n+j}+P_{m+i,n-j}) + \frac{\omega^2}{v^2}\sum_{i=0}^{N_x}\sum_{j=0}^{N_z} b_{i,j}(P_{m-i,n-j}+P_{m+i,n+j}+P_{m-i,n+j}+P_{m+i,n-j}) = 0, \quad (5)$$

where $a_{i,j}$ satisfy $\sum_{i=0}^{N_x}\sum_{j=0}^{N_z} a_{i,j} = 0$.

To perform the dispersion analysis, we substitute a plane wave $P(x,z,\omega) = P_0 e^{-i(k_x x + k_z z)}$ into equation 5. The normalized phase velocity is obtained as

$$\frac{V_{\text{ph}}}{v} = \frac{G}{2\pi}\sqrt{-\frac{\sum_{i=0}^{N_x}\sum_{j=0}^{N_z} a_{i,j}T_{i,j}}{\sum_{i=0}^{N_x}\sum_{j=0}^{N_z} b_{i,j}T_{i,j}}}, \quad (6)$$

where V_{ph} is the phase velocity and $T_{i,j} = \cos(i(2\pi \sin\theta/G))\cos(j(2\pi\cos\theta/rG))$. The number of grid points per wavelength G is defined with respect to the larger spatial sampling interval $\max(\Delta x, \Delta z)$. For the case $\Delta x \geq \Delta z$, $G = 2\pi/k\Delta x$. The term θ is the propagation angle from the z-axis and satisfies $k_x = k \cdot \sin\theta$, $k_z = k \cdot \cos\theta$. The coefficients $a_{i,j}$ and $b_{i,j}$ are determined by minimizing the phase error

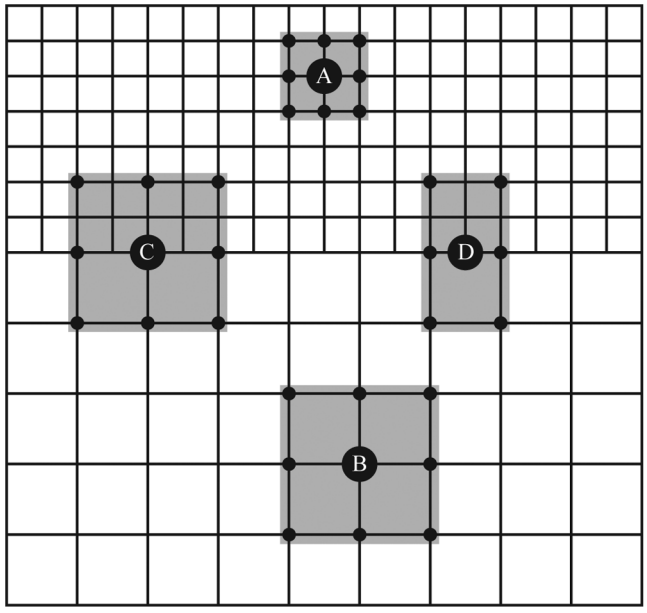

Figure 2. Discontinuous-grid configuration for the 9-point scheme, where points A and B are located in the fine- and coarse-grid regions and points C and D involve special stencils in the transition zone.

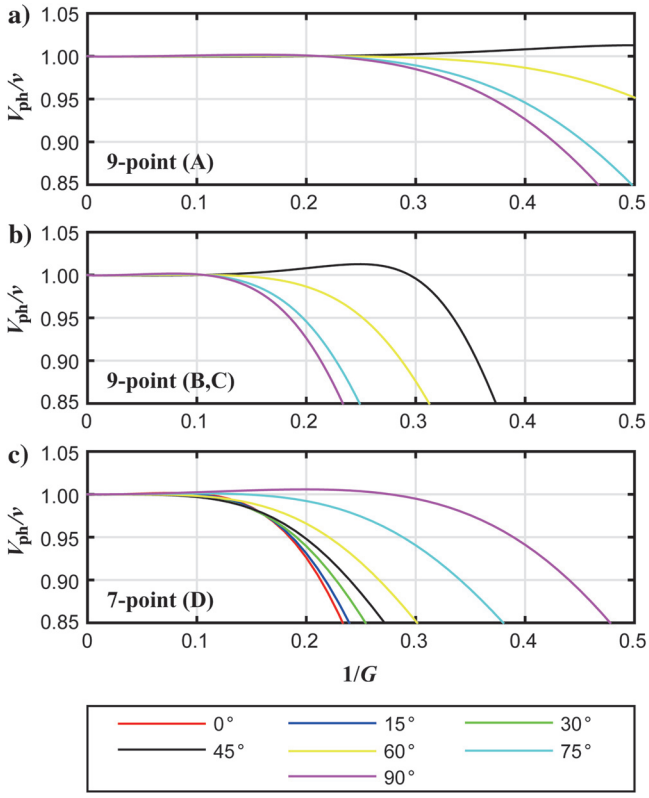

Figure 3. Dispersion curves for different FDFD stencils are shown in Figure 2. (a) 9-point scheme located at A, (b) 9-point schemes located at B and C, and (c) 7-point scheme located at C.

Table 1. Coefficients of different FDFD operators for the discontinuous-grid 9-point scheme.

Scheme	Subscripts	b	c	d
9-point	1, 0	4.42152228426023E-02	3.97801381256927E-01	−1.00989396183610E-01
	0, 1	4.42152227141390E-02	−1.00989537605994E-01	3.97801522922021E-01
	1, 1	1.82555415547753E-03	1.01316785228176E-01	1.01316622117084E-01
7-point	1, 0	2.84805973233173E-03	4.93757076638540E-01	−1.18716232776188E-01
	1, 2	4.59912033498720E-02	−1.47788701711940E-03	1.26355311671418E-01

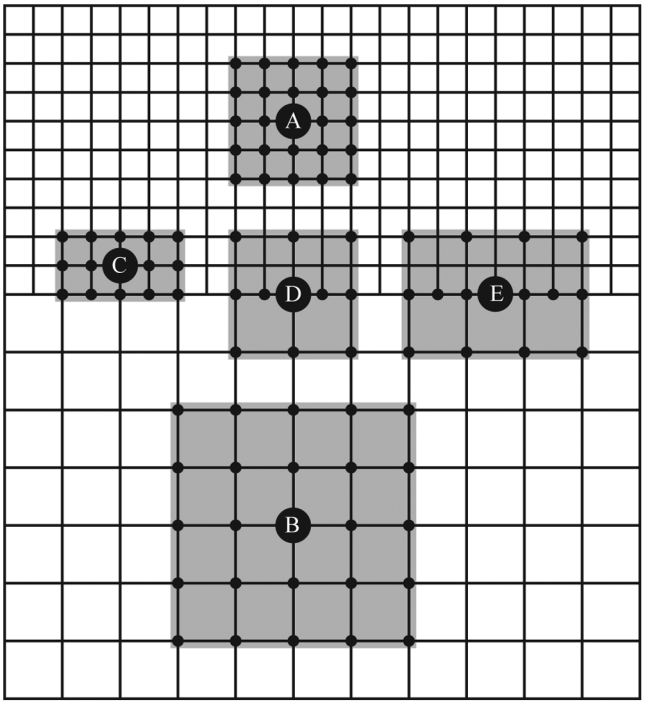

Figure 4. Discontinuous-grid configuration for the 25-point scheme.

$$E(a_{i,j}, b_{i,j}) = \iint \left[1 - \frac{V_{\mathrm{ph}}}{v}\right]^2 d\tilde{k} d\theta, \tag{7}$$

where $\tilde{k} = 1/G$. Given an FDFD stencil, the range of propagation angle θ is $[0, \pi/2]$, and the range of $\tilde{k}$ can be determined by considering the trade-off between the wavenumber coverage and the allowed phase-velocity error (Chen, 2014; Fan et al., 2017). To implement the absorbing boundary, independent coefficients $c_{i,j}$ and $d_{i,j}$ are required. According to Fan et al. (2017), we create the following two functions:

$$E_1 = \frac{\sum_{i=0}^{N_x} \sum_{j=0}^{N_z} c_{i,j} T_{i,j}}{\sum_{i=0}^{N_x} \sum_{j=0}^{N_z} b_{i,j} T_{i,j}} + \left(\frac{2\pi \sin\theta}{G}\right)^2 \tag{8a}$$

and

$$E_2 = \frac{\sum_{i=0}^{N_x} \sum_{j=0}^{N_z} d_{i,j} T_{i,j}}{\sum_{i=0}^{N_i} \sum_{j=0}^{N_j} b_{i,j} T_{i,j}} + \left(\frac{2\pi \cos\theta}{rG}\right)^2. \tag{8b}$$

Parameters $c_{i,j}$ and $d_{i,j}$ (already satisfy $a_{i,j} = c_{i,j} + r^2 d_{i,j}$) can be determined by minimizing the error function:

Table 2. Coefficients of different FDFD operators for the discontinuous-grid 25-point scheme.

Scheme	Subscripts	b	c	d
25-point	1, 0	5.78217827298346E-02	5.60727265402464E-02	−8.66542781092547E-02
	0, 1	5.78217684314893E-02	−8.66546890805362E-02	5.60732273483046E-02
	1, 1	5.21229867820672E-02	4.02036844291894E-02	4.02029913734037E-02
	2, 0	3.49939267487124E-03	5.02478602281297E-02	−4.03002251016512E-03
	0, 2	3.49939019117563E-03	−4.02980887453836E-03	5.02476311551104E-02
	2, 1	4.09067953478049E-03	4.62843358770098E-02	−1.21719466335537E-04
	1, 2	4.09067716185693E-03	−1.22010028175578E-04	4.62846184593161E-02
	2, 2	5.22403718311664E-05	4.27351493102198E-03	4.27347226989979E-03
15-point (C)	1, 0	8.92761632779835E-02	8.66592897676037E-02	−2.15164250441208E-01
	2, 0	6.81831558897478E-03	7.86534894068312E-02	−1.95908261285839E-02
	0, 1	2.45615839405423E-02	−4.11149743015129E-02	2.63917386391569E-01
	1, 1	2.37729589191511E-02	2.15365282968781E-02	2.14677683469774E-01
	2, 1	3.20519169186576E-05	1.92574329161197E-02	1.98849759538215E-02
11-point	1, 0	2.10600100347608E-01	−5.22392789034492E-01	−8.97137170303385E-03
	2, 0	9.62317792145256E-03	2.33146018008485E-01	−3.98401060937905E-02
	0, 2	3.55625145498464E-02	-2.24534583967475E-02	8.23027373052518E-02
	2, 2	1.28483890247018E-02	2.22178529671989E-02	4.24549690179896E-02
15-point (E)	1, 0	6.32384653959232E-02	3.33545210163886E-01	−2.66843786731160E-01
	2, 0	4.15911499069887E-02	−1.16346746479054E-01	6.75668724527263E-02
	3, 0	6.66369535971710E-03	5.86885255533620E-02	−2.02296930435190E-02
	1, 2	4.77085692761939E-02	−1.34338019141954E-02	1.18178680156804E-01
	3, 2	6.35223285305913E-04	1.34548272209029E-02	6.33753099351924E-03

$$E = \iint (E_1^2 + E_2^2) d\tilde{k} d\theta, \tag{9}$$

where the ranges of θ and $\tilde{k}$ are the same as those in equation 7.

Equation 4 is the general formula for a $(2N_x + 1) \times (2N_z + 1)$-point scheme. Actually, $3[(N_x + 1) \times (N_z + 1) - 1]$ independent coefficients can be determined by optimizing equations 7 and 9. For some special FDFD stencils such as the 17-point scheme (Tang et al., 2015), when the coefficients at certain points are zero, only the nonzero coefficients need be optimized. The optimization process used here is essentially the same as that used in Fan et al. (2017). However, due to different combinations of coefficients used, some optimal coefficients here are different from those in Fan et al. (2017) by an integer factor of two or four.

The methodology of discontinuous-grid FDFD scheme

The subsurface media usually have lower velocity in a shallow region and higher velocity in a deep region. To adapt to velocity variations like this, it is expected that we can use fine and coarse grids in different regions, as shown in Figure 2. Assuming that the horizontal and vertical grid intervals are Δx and Δz in the fine-gridded region and $2\Delta x$ and $2\Delta z$ in the coarse-gridded region, the coarse-to-fine grid spacing ratio N equals to two. We first consider the 9-point discontinuous-grid FDFD scheme. Illustrated in Figure 2 are some typical stencils involved in coarse, fine, and transition regions. The standard 9-point schemes are used in the fine and coarse grid regions (as indicated by A and B in Figure 2). The key issue is that a particular FDFD operator should be used in regions where the fine grid is connecting to the coarse grid. Two types of grid points are involved in that row. The first is the grid point centered at C, where the vertical grid line is continuous and the standard 9-point scheme can be used. The second is the grid point centered at D, where the vertical grid line is discontinuous and a new 7-point scheme is formed.

The optimal coefficients for 9- and 7-point schemes can be calculated using the same optimal method mentioned above. To optimize objective functions in equations 7 and 9, we set the range of $\tilde{k}$ within [0, 0.25] for 9-point scheme and [0, 0.10] for 7-point scheme. The resulting coefficients are listed in Table 1, and the normalized phase velocities are illustrated in Figure 3. Shown in Figure 3a are dispersion curves for the standard 9-point stencil at grid point A. The dispersion curves for the 9-point stencils at grid points B and C (Figure 3b) are obtained by shrinking the dispersion curves of the 9-point (A) by half along the horizontal axis because the spatial interval is $2\Delta x$ and $2\Delta z$. Shown in Figure 3c are dispersion curves for the 7-point stencil at grid point C. The 1% phase-velocity error is a widely used criterion to determine the minimum G for different FDFD operators. The maximum $1/G$s for the stencils in Figure 3a–3c are 0.29, 0.145, and 0.135, respectively. Because stencils B-D are used in the lower layer, where the speed is at least twice of that in the upper layer, the wavelength there is at least twice longer than in the upper layer. Then, the maximum $1/G$s for the latter two stencils are actually 0.29 and 0.27. Therefore, to keep the phase-velocity error less than 1%, G should be at least 3.70 for the 9-point discontinuous-grid scheme.

In addition to the 9-point scheme, we also develop a discontinuous grid for a 25-point FDFD scheme, which is widely used for its lower spatial dispersion. Illustrated in Figure 4 are typical stencils involved in different regions. The standard 25-point scheme can be used inside the fine- and coarse-grid regions (as indicated by A and B). On the other hand, special operators are used in the transition region. Because the 25-point scheme involves more rows of grid points, its transition zone involves more rows. Along the row above the connecting row, a 15-point scheme (indicated by C) is used. At the connecting row, two kinds of stencils are used, an 11-point scheme at grid point D and another 15-point scheme at grid point E.

The optimal coefficients for these schemes can be calculated by the same method used before. To optimize objective functions in equations 7 and 9, we set the range of $\tilde{k}$ within [0, 0.45] for the 25-point scheme, [0, 0.30] for the 15-point scheme (C), [0, 0.15] for

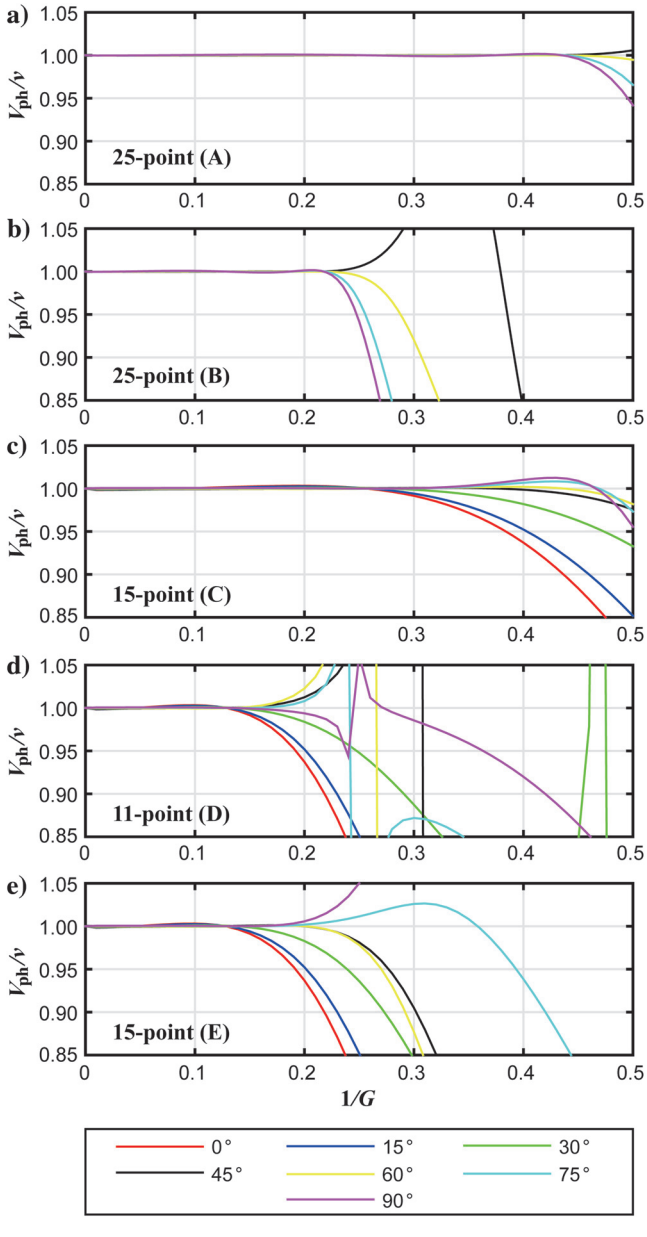

Figure 5. Dispersion curves for different FDFD stencils are shown in Figure 4. (a-e) 25-point scheme (location A), 25-point scheme (location B), 15-point scheme (location C), 11-point scheme (location D), and another 15-point scheme (location E), respectively.

the 11-point scheme, and [0, 0.15] for another 15-point scheme (E). The resulting optimized coefficients are listed in Table 2, and the related normalized phase velocities are illustrated in Figure 5. Similar to the analysis of Figure 3, the maximum $1/G$s for difference stencils in Figure 5a–5e are 0.47, 0.235, 0.31, 0.16, and 0.16, respectively. Stencils B-E are used in the lower layer, where the speed is at least twice that in the upper layer. The maximum $1/G$s for the four stencils are actually 0.47, 0.61, 0.32, and 0.32, respectively. Therefore, to keep the phase-velocity error less than 1%, the G should be at least 3.125 for the 25-point discontinuous-grid scheme.

The computational efficiency of FDFD modeling is primarily dependent on the size and sparsity of the impedance matrix (Štekl and Pratt, 1998). As an example, we use a simple model to compare the impedance matrices of the uniform and discontinuous grids. The model is partitioned in two ways, a uniform grid with 11×15 grid points (Figure 6a) and a discontinuous grid consisting of 11×5 grid points in its top part and 6×5 grid points in its bottom part (Figure 6b). The 9- and 25-point schemes are tested for the uniform and discontinuous grids, and structures of their impedance matrices are compared in Figure 6c–6f. Compared with the uniform grid, the discontinuous gird reduces the size of the impedance matrix to 26.5% for the 9- and 25-point schemes, reduces the nonzero elements to 48.6% for the 9-point scheme, and to 41.1% for the 25-point scheme. For both schemes, the size and sparsity of the impedance matrix are greatly reduced.

To check whether changing the structure of the impedance matrix can cause the linear system to be ill-conditioned, we calculate condition numbers for the above example. They are 3.283 and 3.026 for the uniform- and discontinuous-grid 9-point schemes and 81.07 and 49.16 for the uniform- and discontinuous-grid 25-point schemes. The condition number of the discontinuous-grid method is smaller than that of the corresponding uniform-grid method, for the 9- and 25-point schemes. Therefore, the linear problem is still well-conditioned.

The above discontinuous-grid FDFD method is derived based on $N = 2$. Following the approach by Fan et al. (2015) for the TDFD, this procedure can be repeated n times to achieve an overall factor of $N = 2^n$ by successively using multiple transition zones. However, this scheme cannot be extended to numbers other than a power of 2, for example, $N = 3$.

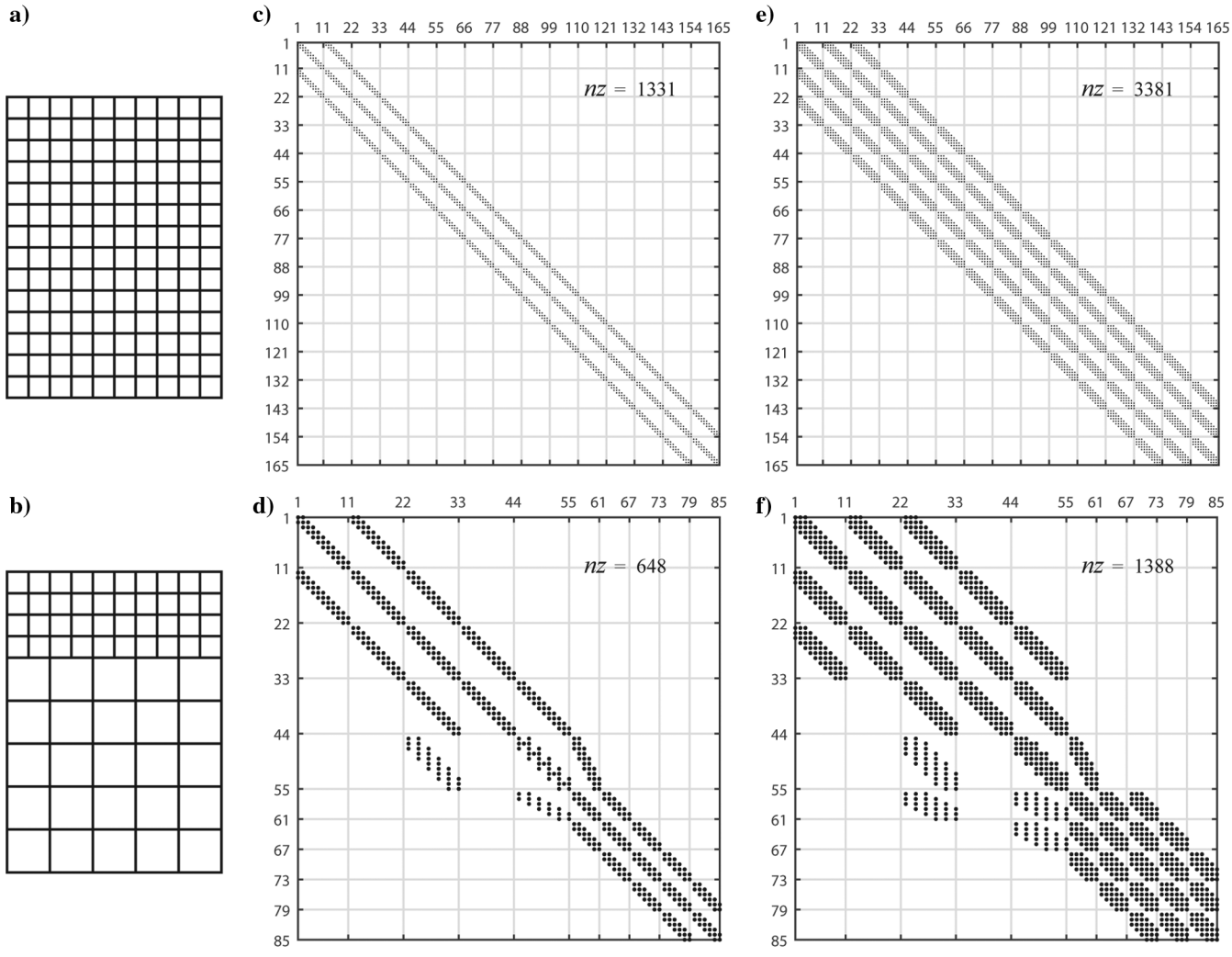

Figure 6. Impedance matrices for the 9- and 25-point schemes. (a and b) Different partitions using uniform and discontinuous grids in the same model. (c and e) Impedance matrices for 9- and 25-point schemes using the uniform grid. (d and f) Impedance matrices for 9- and 25-point schemes using the discontinuous grid.

NUMERICAL EXAMPLES

To validate the accuracy and efficiency of the proposed discontinuous-grid FDFD method, we compare numerical results calculated using our method with those from the conventional uniform-grid method using 9- and 25-point schemes. The sparse linear systems involved in all numerical examples are solved using LU decomposition of the impedance matrix. The subsequent Gaussian elimination is calculated using the open-source software MUMPS (multifrontal massively parallel solver, Amestoy et al., 2001, 2006). The first model tested is a 2D homogeneous model with a size of 3000×3000 m and a constant velocity of 4000 m/s. The source is a 30 Hz Ricker wavelet located at the center of the model (1500, 1500 m). The model is discretized by either a uniform grid or a discontinuous grid, respectively. The former uses a small grid spacing of $\Delta x = \Delta z = 7.5$ m in the entire model and results in a grid size of 401×401. The latter uses a small grid spacing of $\Delta x = \Delta z = 7.5$ m in the shallow part and a large grid spacing of $2\Delta x$ and $2\Delta z$ in the deeper part. The boundary between the two differently gridded regions stays at $z = 1650$ m (indicated by a dashed line in Figures 7b and 8b), and the sizes of the finely and coarsely gridded regions are 401×221 and 201×90. Then, the two differently gridded models are used to work with the 9- and 25-point schemes, and the corresponding results are shown in Figures 7 and 8. Figure 7a and 7b shows wavefield snapshots at $t = 0.36$ s for the uniform-grid and discontinuous-grid 9-point schemes. Figure 7c and 7d compares synthetic seismograms from two receivers located at (1500, 1350 m) and (1500, 1950 m). Figure 8 is similar to Figure 7 except that the 25-point scheme is used. By comparing snapshots and seismograms, we find that, for the 9- and 25-point schemes, the discontinuous-grid scheme has nearly the same accuracy as the conventional uniform-grid scheme. As for the memory requirement and computational efficiency, they mainly depend on the structure of the impedance matrix. For this specific example (including the perfectly matched layers), the discontinuous-grid method reduces the size of the matrix to 42.6%, the number of nonzero elements to 65.2% and 65.1% for the 9- and 25-point schemes, respectively. The CPU times are 632 and 389 s for the uniform-grid and discontinuous-grid 9-point schemes, and 1468 and 824 s for the uniform-grid and discontinuous-grid 25-point schemes, respectively. Apparently, the discontinuous-grid method can greatly reduce the computational cost for the 9- and 25-point schemes.

The second is a three-layer model with a size of 1000×1000 m. The velocities in the three layers are 1000, 2000, and 4000 m/s, with the two interfaces located at $z = 250$ and 650 m. The source is a

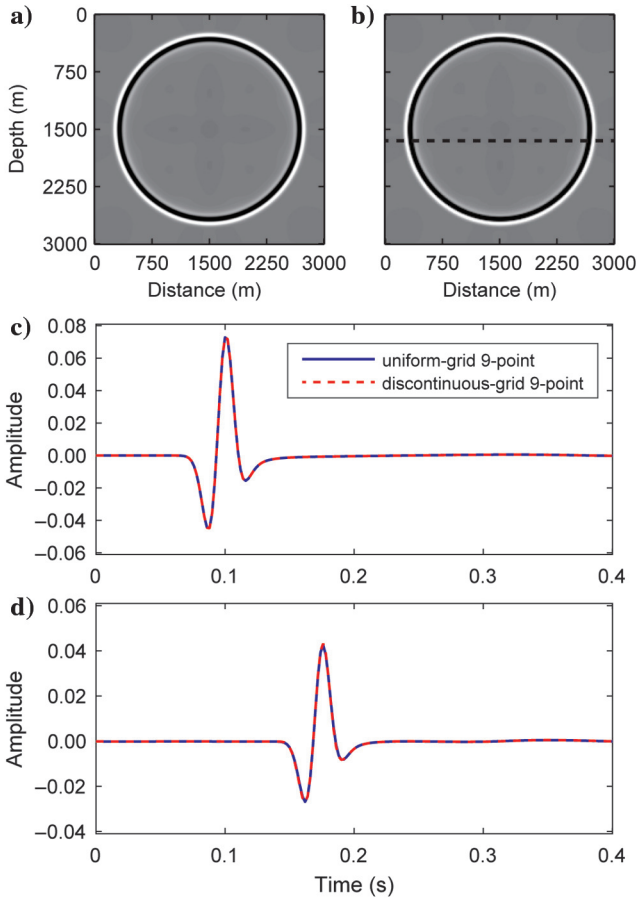

Figure 7. Simulation results using the homogeneous velocity model and the uniform-grid and discontinuous-grid 9-point schemes. (a and b) Wavefield snapshots at $t = 0.36$ s for the uniform-grid and discontinuous-grid 9-point schemes, respectively. The dashed line in (b) denotes the boundary between the fine and coarse grids. (c and d) Synthetic seismograms calculated at (1500, 1350 m) and (1500, 1950 m) using a uniform grid (solid blue line) and a discontinuous grid (dashed red line), respectively.

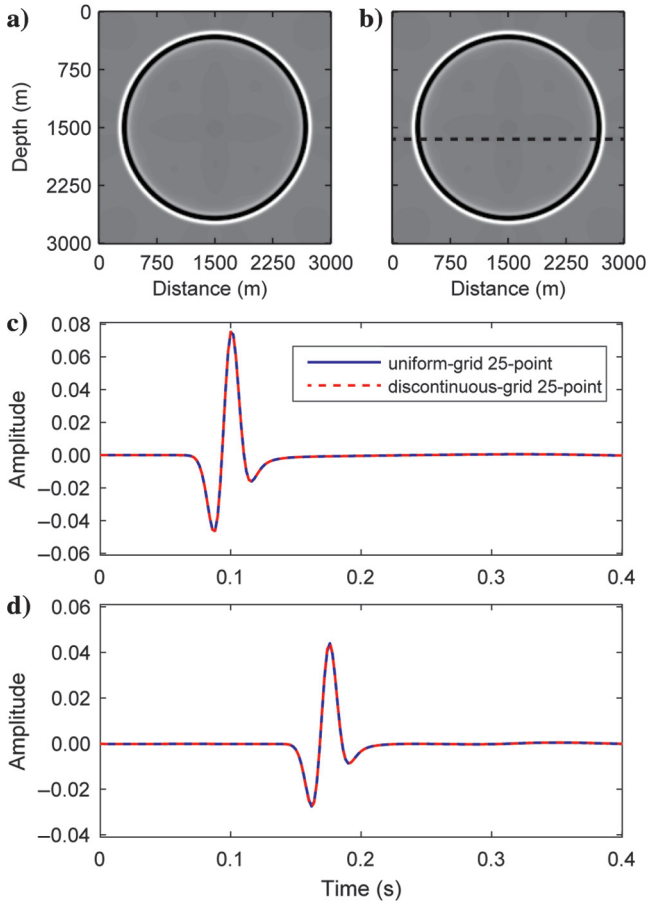

Figure 8. Similar to Figure 7, except the results are calculated using uniform-grid and discontinuous-grid 25-point schemes.

30 Hz Ricker wavelet located at (500, 400 m). The layered model is discretized by the uniform-grid and the discontinuous-grid, respectively. The former uses a small grid spacing of $\Delta x = \Delta z = 2.5$ m in the entire model. The latter uses $\Delta x = \Delta z = 2.5$ m between $z = 0$ and 242.5 m, $2\Delta x$ and $2\Delta z$ between $z = 242.5$ and 630 m, and $4\Delta x$ and $4\Delta z$ at deeper than $z = 630$ m. The borders between the three differently gridded regions are indicated by dashed lines in Figures 9b and 10b. Three receivers are placed in the three differently gridded regions at (500, 125 m), (700, 400 m), and (500, 800 m),

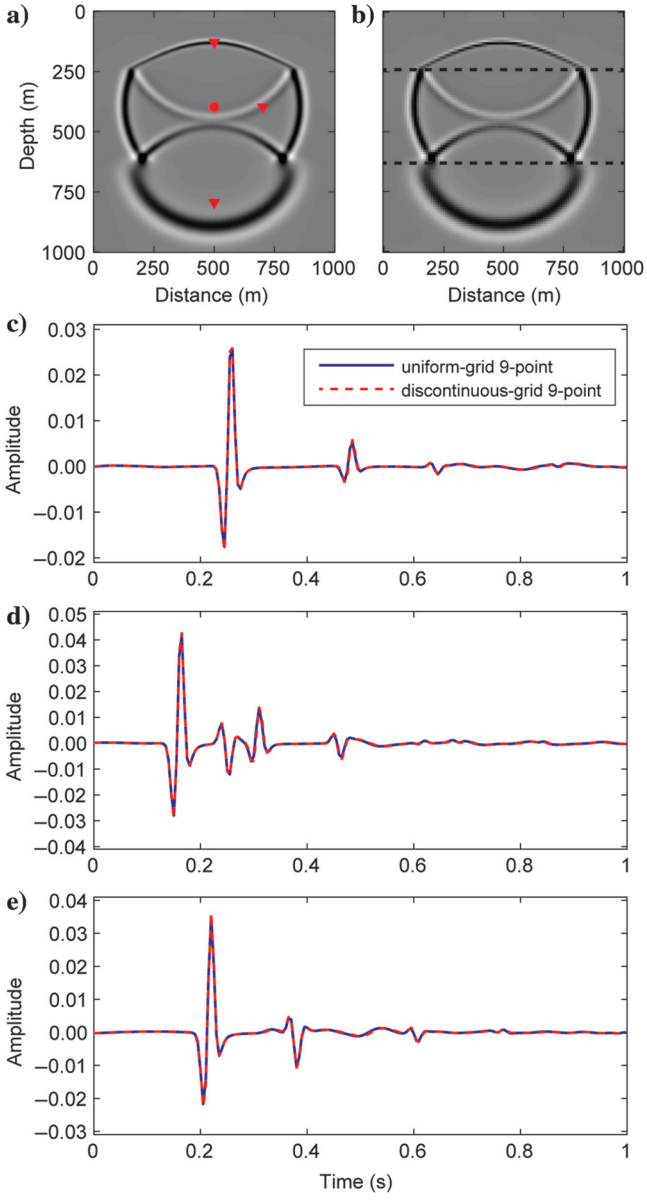

Figure 9. Simulation results using the three-layer model and uniform-grid and discontinuous-grid 9-point schemes. (a and b) Wavefield snapshots at $t = 0.25$ s. The two dashed lines in (b) denote the boundaries between the different grids. Shown in (c-e) are seismograms calculated at locations (500, 125 m), (700, 400 m), and (500, 800 m), using the uniform-grid (solid blue line) and discontinuous-grid (dashed red line) methods. The locations of the source and three receivers are indicated by the red star and triangles in (a).

respectively (Figure 9a and 10a). The two differently gridded models are then used to work with the 9- and 25-point schemes. The corresponding results are shown in Figures 9 and 10. Figure 9a and 9b shows the wavefield snapshots at $t = 0.25$ s for the uniform-grid and discontinuous-grid 9-point schemes. Figure 9c–9e compares seismograms at three receivers. Figure 10 is similar to Figure 9 except that the 25-point scheme is used. From Figures 9 and 10, the results demonstrate that, for the three-layer model, the discontinuous-grid and uniform-grid schemes generate comparable accuracy, regardless of using the 9- or 25-point scheme. Regarding memory requirements and computational efficiency, the discontinuous-grid reduces the size of the matrix to 17.5% and the number of nonzero elements to 41.8% and 41.6% for the 9- and 25-point schemes, respectively. The CPU times are 623 and 243 s for the uniform- and

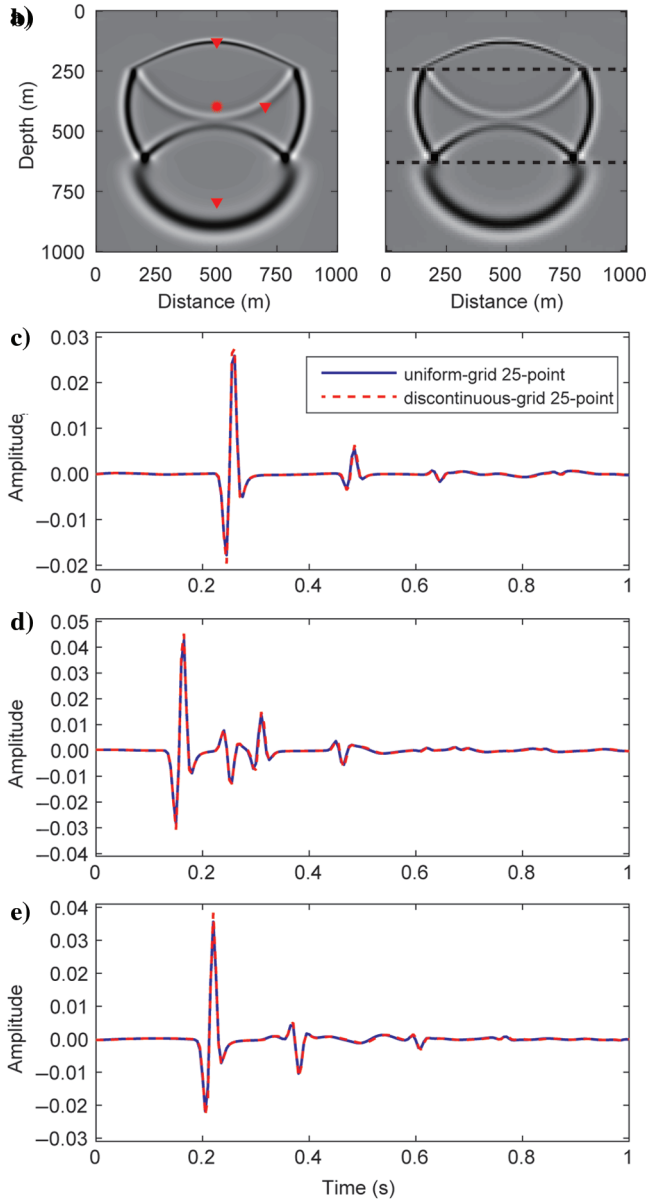

Figure 10. Similar to those in Figure 9, except the uniform-grid and discontinuous-grid 25-point schemes are used.

discontinuous-grid 9-point schemes and 1462 and 486 s for the uniform- and discontinuous-grid 25-point schemes, respectively. Similar to the test in the homogeneous model, the discontinuous-grid method requires much less computational cost for both 9- and 25-point schemes. From the above two numerical examples, we see that the discontinuous-grid method can greatly reduce the computational cost while keeping the accuracy comparable to the uniform-grid scheme. Although increasing the efficiency is mainly dependent on the reduction of the impedance matrix, number of nonzero elements, and characteristics of velocity models, the specific solvers used may also affect its actual performance.

Instability problems used to happen in time-domain discontinuous-grid modeling (Kristek et al., 2010; Zhang et al., 2013; Fan et al., 2015). We implement another numerical experiment to test this issue in frequency-domain discontinuous-grid modeling. The discontinuous-grid 9-point scheme is used to calculate synthetic seismograms in a homogeneous medium. The model size, discretization, velocity, and source location are the same as those used in the first numerical example. To test the stability of the frequency-domain method, an extremely large number of time steps 2^{15} and a time-sampling interval of 0.005 s are used. This is equivalent to a frequency interval of approximately 6.1×10^{-3} Hz. For coarse-to-fine-grid spacing ratios $N = 2$ and 4, seismograms received at (1500, 1475 m) are illustrated in Figure 11a and 11b. To demonstrate the waveform accuracy and stability after a very long elapsed time, the inset plots give magnified waveforms for the first one second, whereas the waveforms below them give the full length of calculations up to 164 s. We see seismograms stay stable within the entire time span. Although not shown here, similar results can be obtained using the discontinuous-grid 25-point scheme. Frequency-domain methods are naturally resistant against time instability problem. This is mainly because, unlike the time-domain method, the frequency-domain method does not have time dispersion.

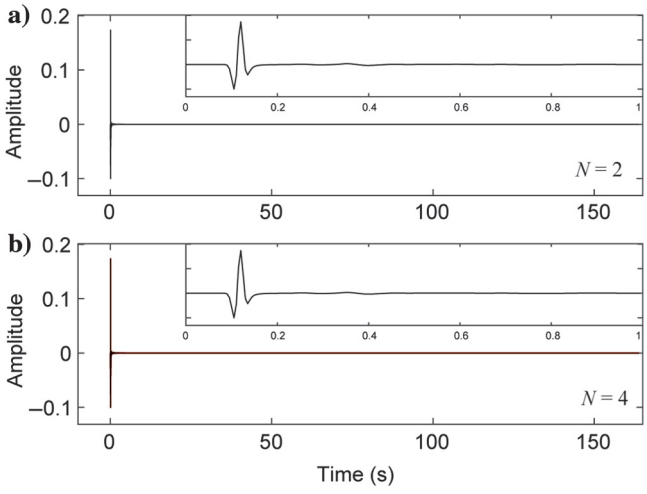

Figure 11. Examples for the numerical stability test. Synthetic seismograms are calculated using the discontinuous-grid 9-point scheme for grid spacing ratios (a) $N = 2$ and (b) 4. The inset plots show waveform details by magnified waveforms within the first 1 s. The full seismograms are extended to 164 s to illustrate the stability at an extremely long time.

CONCLUSION

The discontinuous-grid method usually works in time-domain FD modeling. In this study, we proposed a discontinuous-grid finite-difference scheme for frequency-domain 2D scalar wave equation. Special FD stencils are designed to fit the shape of the FDFD operator in the transition zone between different gridded regions. Optimization procedures were derived to find the expansion coefficients for the discontinuous-grid 9- and 25-point schemes. The ratio of grid intervals changing from coarse-to-fine can be any number equals to a power of two. Numerical experiments demonstrated that the proposed discontinuous-grid scheme for FDFD modeling yields wavefields that are comparable with those using conventional uniform-grid simulations, while greatly reducing memory and computational costs for models with large velocity contrast. The stability problem often seen in the TDFD discontinuous-grid method does not happen for FDFD. The potential applications of the discontinuous grid in finite-difference calculations and its actual savings in computational cost are closely related to the characteristics of velocity models. This method is suitable for models with a large-scale velocity variation trend, e.g., regions with a strong vertical velocity gradient. It may also be useful in some special models in which a large amount of small-scale low-velocity inclusions are embedded in a layer. Examples of such models include an intermediate layer with gas clouds or a shallow low-velocity layer composed of strong heterogeneities generating near-surface scatterings.

ACKNOWLEDGMENTS

The editors and three anonymous reviewers are appreciated for their comments that greatly improved this paper. This research is financially supported by the National Natural Science Foundation of China (grant nos. 41604037 and 41602132).

REFERENCES

Amestoy, P. R., I. S. Duff, J. Y. L'Excellent, and J. Koster, 2001, A fully asynchronous multifrontal solver using distributed dynamic scheduling: Journal on Matrix Analysis and Applications, **23**, 15–41, doi: 10.1137/S0895479899358194.

Amestoy, P. R., J. Y. Guermouche, H. L'Excellent, and S. Pralet, 2006, Hybrid scheduling for the parallel solution of linear systems: Parallel computing, **32**, 136–156, doi: 10.1016/j.parco.2005.07.004.

Aoi, S., and H. Fujiwara, 1999, 3D finite-difference method using discontinuous grids: Bulletin of the Seismological Society of America, **89**, 918–930.

Brossier, R., S. Operto, and J. Virieux, 2009, Seismic imaging of complex onshore structures by 2D elastic frequency-domain full-waveform inversion: Geophysics, **74**, no. 6, WCC105–WCC118, doi: 10.1190/1.3215771.

Cao, S.-H., and J.-B. Chen, 2012, A 17-point scheme and its numerical implementation for high-accuracy modeling of frequency-domain acoustic equation (in Chinese): Chinese Journal of Geophysics, **55**, 239–251, doi: 10.1002/cjg2.v55.2.

Chen, J.-B., 2012, An average-derivative optimal scheme for frequency-domain scalar wave equation: Geophysics, **77**, no. 6, T201–T210, doi: 10.1190/geo2011-0389.1.

Chen, J.-B., 2014, A 27-point scheme for a 3D frequency-domain scalar wave equation based on an average-derivative method: Geophysical Prospecting, **62**, 258–277, doi: 10.1111/1365-2478.12090.

Chen, J.-B., and J. Cao, 2016, Modeling of frequency-domain elastic-wave equation with an average-derivative optimal method: Geophysics, **81**, no. 6, T339–T356, doi: 10.1190/geo2016-0041.1.

Falk, J., E. Tessmer, and D. Gajewski, 1998, Efficient finite-difference modeling of seismic waves using locally adjustable time steps: Geophysical Prospecting, **46**, 603–616, doi: 10.1046/j.1365-2478.1998.00110.x.

Fan, N., L.-F. Zhao, Y.-J. Gao, and Z.-X. Yao, 2015, A discontinuous collocated-grid implementation for high-order finite-difference modeling: Geophysics, **80**, no. 4, T175–T181, doi: 10.1190/geo2015-0001.1.

Fan, N., L.-F. Zhao, X.-B. Xie, X.-G. Tang, and Z.-X. Yao, 2017, A general optimal method for 2D frequency-domain finite-difference solution of scalar wave equation: Geophysics, **82**, no. 3, T121–T132, doi: 10.1190/geo2016-0457.1.

Fichtner, A., J. Trampert, P. Cupillard, E. Saygin, T. Taymaz, Y. Capdeville, and A. Villaseñor, 2013, Multiscale full waveform inversion: Geophysical Journal International, **194**, 534–556, doi: 10.1093/gji/ggt118.

Fornberg, B., and N. Flyer, 2015, Fast generation of 2-D node distributions for mesh-free PDE discretizations: Computers and Mathematics with Applications, **69**, 531–544, doi: 10.1016/j.camwa.2015.01.009.

Gosselin-Cliche, B., and B. Giroux, 2014, 3D frequency-domain finite-difference viscoelastic-wave modeling using weighted average 27-point operators with optimal coefficients: Geophysics, **79**, no. 3, T169–T188, doi: 10.1190/geo2013-0368.1.

Gu, B., G. Liang, and Z. Li, 2013, A 21-point finite difference scheme for 2D frequency-domain elastic wave modeling: Exploration Geophysics, **44**, 156–166, doi: 10.1071/EG12064.

Hayashi, K., D. R. Burns, and M. N. Toksöz, 2001, Discontinuous-grid finite-difference seismic modeling including surface topography: Bulletin of the Seismological Society of America, **91**, 1750–1764, doi: 10.1785/0120000024.

Hu, J., and X. Jia, 2016, Numerical modeling of seismic waves using frequency-adaptive meshes: Journal of Applied Geophysics, **131**, 41–53, doi: 10.1016/j.jappgeo.2016.05.011.

Huang, C., and L.-G. Dong, 2009a, High-order finite-difference method in seismic wave simulation with variable grids and local time-steps (in Chinese): Chinese Journal of Geophysics, **52**, 176–187, doi: 10.1002/cjg2.v52.1.

Huang, C., and L.-G. Dong, 2009b, Staggered-grid high-order finite-difference method in elastic wave simulation with variable grids and local time-steps (in Chinese): Chinese Journal of Geophysics, **52**, 1324–1333, doi: 10.1002/cjg2.1457.

Hustedt, B., S. Operto, and J. Virieux, 2004, Mixed-grid and staggered-grid finite-difference methods for frequency-domain acoustic wave modeling: Geophysical Journal International, **157**, 1269–1296, doi: 10.1111/j.1365-246X.2004.02289.x.

Jastram, C., and A. Behle, 1992, Acoustic modeling on a grid of vertically varying spacing: Geophysical Prospecting, **40**, 157–169, doi: 10.1111/j.1365-2478.1992.tb00369.x.

Jastram, C., and E. Tessmer, 1994, Elastic modeling on a grid with vertically varying spacing: Geophysical Prospecting, **42**, 357–370, doi: 10.1111/j.1365-2478.1994.tb00215.x.

Jo, C.-H., C. Shin, and J. H. Suh, 1996, An optimal 9-point, finite-difference, frequency-space, 2-D scalar wave extrapolator: Geophysics, **61**, 529–537, doi: 10.1190/1.1443979.

Kang, T.-S., and C.-E. Baag, 2004, Finite-difference seismic simulation combining discontinuous grids with locally variable timesteps: Bulletin of the Seismological Society of America, **94**, 207–219, doi: 10.1785/0120030080.

Kim, Y., D.-J. Min, and C. Shin, 2011, Frequency-domain reverse-time migration with source estimation: Geophysics, **76**, no. 2, S41–S49, doi: 10.1190/1.3534831.

Kristek, J., P. Moczo, and M. Galis, 2010, Stable discontinuous staggered grid in the finite-difference modelling of seismic motion: Geophysical Journal International, **183**, 1401–1407, doi: 10.1111/j.1365-246X.2010.04775.x.

Li, B., Y. Liu, M. K. Sen, and Z. Ren, 2017, Time-space-domain mesh-free finite difference based on least squares for 2D acoustic-wave modeling: Geophysics, **82**, no. 4, T143–T157, doi: 10.1190/geo2016-0464.1.

Li, H., W. Zhang, Z. Zhang, and X. Chen, 2015, Elastic wave finite-difference simulation using discontinuous curvilinear grid with non-uniform time step: Two-dimensional case: Geophysical Journal International, **202**, 102–118, doi: 10.1093/gji/ggv129.

Li, Y., B. Han, L. Métivier, and R. Brossier, 2016, Optimal fourth-order staggered-grid finite-difference scheme for 3D frequency-domain viscoelastic wave modeling: Journal of Computational Physics, **321**, 1055–1078, doi: 10.1016/j.jcp.2016.06.018.

Loewenthal, D., and I. R. Mufti, 1983, Reversed time migration in spatial frequency domain: Geophysics, **48**, 627–635, doi: 10.1190/1.1441493.

Martin, B., B. Fornberg, and A. St-Cy, 2015, Seismic modeling with radial-basis-function-generated finite differences: Geophysics, **80**, no. 4, T137–T146, doi: 10.1190/geo2014-0492.1.

Min, D.-J., C. Shin, B.-D. Kwon, and S. Chung, 2000, Improved frequency-domain elastic wave modeling using weighted-averaging difference operators: Geophysics, **65**, 884–895, doi: 10.1190/1.1444785.

Operto, S., R. Brossier, L. Combe, L. Métivier, A. Ribodetti, and J. Virieux, 2014, Computationally efficient three-dimensional acoustic finite-difference frequency-domain seismic modeling in vertical transversely isotropic media with sparse direct solver: Geophysics, **79**, no. 5, T257–T275, doi: 10.1190/geo2013-0478.1.

Operto, S., J. Virieux, P. Amestoy, J.-Y. L'Excellent, L. Giraud, and H. B. H. Ali, 2007, 3D finite-difference frequency-domain modeling of visco-acoustic wave propagation using a massively parallel direct solver: A feasibility study: Geophysics, **72**, no. 5, SM195–SM211, doi: 10.1190/1.2759835.

Operto, S., J. Virieux, A. Ribodetti, and J. E. Anderson, 2009, Finite-difference frequency-domain modeling of viscoacoustic wave propagation in 2D tilted transversely isotropic (TTI) media: Geophysics, **74**, no. 5, T75–T95, doi: 10.1190/1.3157243.

Plessix, R.-E., and W. Mulder, 2004, Frequency-domain finite-difference amplitude-preserving migration: Geophysical Journal International, **157**, 975–987, doi: 10.1111/j.1365-246X.2004.02282.x.

Pratt, R. G., 1999, Seismic waveform inversion in the frequency domain. Part 1: Theory and verification in a physical scale model: Geophysics, **64**, 888–901, doi: 10.1190/1.1444597.

Shin, C., and H. Sohn, 1998, A frequency-space 2-D scalar wave extrapolator using extended 25-point finite-difference operator: Geophysics, **63**, 289–296, doi: 10.1190/1.1444323.

Štekl, I., and R. G. Pratt, 1998, Accurate viscoelastic modeling by frequency-domain finite differences using rotated operators: Geophysics, **63**, 1779–1794, doi: 10.1190/1.1444472.

Takekawa, J., and H. Mikada, 2016, A mesh-free finite-difference method for frequency-domain viscoacoustic wave equation: 86th Annual International Meeting, SEG, Expanded Abstracts, 3841–3845.

Takekawa, J., H. Mikada, and N. Imamura, 2015, A mesh-free method with arbitrary-order accuracy for acoustic wave: Computers & Geosciences, **78**, 15–25, doi: 10.1016/j.cageo.2015.02.006.

Tang, X., H. Liu, H. Zhang, L. Liu, and Z. Wang, 2015, An adaptable 17-point scheme for high-accuracy frequency-domain acoustic wave modeling in 2D constant density media: Geophysics, **80**, no. 6, T211–T221, doi: 10.1190/geo2014-0124.1.

Tessmer, E., 2000, Seismic finite-difference modeling with spatially varying time steps: Geophysics, **65**, 1290–1293, doi: 10.1190/1.1444820.

Virieux, J., and S. Operto, 2009, An overview of full-waveform inversion in exploration geophysics: Geophysics, **74**, no. 6, WCC1–WCC26, doi: 10.1190/1.3238367.

Wang, Y., and G. T. Schuster, 1996, Finite-difference variable grid scheme for acoustic and elastic wave equation modeling: 66th Annual International Meeting, SEG, Expanded Abstracts, 674–677.

Wang, Y., and H. Takenaka, 2001, A multidomain approach of the Fourier pseudospectral method using discontinuous grid for elastic wave modeling: Earth, Planets and Space, **53**, 149–158, doi: 10.1186/BF03352372.

Wang, Y., J. Xu, and G. T. Schuster, 2001, Viscoelastic wave simulation in basins by a variable-grid finite-difference method: Bulletin of the Seismological Society of America, **91**, 1741–1749, doi: 10.1785/0120000236.

Yang, Q., and W. Mao, 2016, Simulation of seismic wave propagation in 2-D poroelastic media using weighted-averaging finite difference stencils in the frequency-space domain: Geophysical Journal International, **208**, 148–161, doi: 10.1093/gji/ggw380.

Zhang, H., H. Liu, L. Liu, W.-J. Jin, and X.-D. Shi, 2014, Frequency domain acoustic equation high-order modeling based on an average-derivative method (in Chinese): Chinese Journal of Geophysics, **57**, 1599–1611.

Zhang, H., B. Zhang, B. Liu, H. Liu, and X. Shi, 2015, Frequency-space domain high-order modeling based on an average-derivative optimal method: 85th Annual International Meeting, SEG, Expanded Abstracts, 3749–3753.

Zhang, Z., W. Zhang, H. Li, and X. Chen, 2013, Stable discontinuous grid implementation for collocated-grid finite-difference seismic wave modeling: Geophysical Journal International, **192**, 1179–1188, doi: 10.1093/gji/ggs069.